Research Article

Nano Research
2019, 12(11): 2774–2780

ISSN 1998-0124 CN 11-5974/O4
https://doi.org/10.1007/s12274-019-2512-7

2D nanoplate assembled nitrogen doped hollow carbon sphere decorated with Fe_3O_4 as an efficient electrocatalyst for oxygen reduction reaction and Zn-air batteries

Yanqiang Li[1,§] (✉), Huiyong Huang[1,§], Siru Chen[3] (✉), Xin Yu[1], Chao Wang[1], and Tingli Ma[2] (✉)

[1] *State Key Laboratory of Fine Chemicals, School of Petroleum and Chemical Engineering, Dalian University of Technology, Panjin Campus, Panjin 124221, China*
[2] *Graduate School of Life Science and Systems Engineering, Kyushu Institute of Technology, 2-4 Hibikino, Wakamatsu, Kitakyushu, Fukuoka 808-0196, Japan*
[3] *Center for Advanced Materials Research, Zhongyuan University of Technology, Zhengzhou 450007, China*
[§] *Yanqiang Li and Huiyong Huang contributed equally to this work.*

Received: 19 June 2019 / **Revised:** 15 August 2019 / **Accepted:** 2 September 2019

ABSTRACT

Designing a highly efficient non-precious based oxygen reduction reaction (ORR) electrocatalyst is critical for the commercialization of various sustainable energy storage and conversion devices such as metal-air batteries and fuel cells. Herein, we report a convenient strategy to synthesis Fe_3O_4 embedded in N doped hollow carbon sphere (NHCS) for ORR. What's interesting is that the carbon microsphere is composed of two-dimensional (2D) nanoplate that could provide more exposed active sites. The usage of solid ZnO nanowires as zinc source is crucial to obtain this structure. The Fe_3O_4@NHCS-2 exhibits better catalytic activity and durability than the commercial Pt/C catalyst. Moreover, it further displays high-performance of Zn-air batteries as a cathode electrocatalyst with a high-power density of 133 $mW \cdot cm^{-2}$ and high specific capacity of 701 $mA \cdot h \cdot g^{-1}$. The special hollow structure composed 2D nanoplate, high surface area, as well as synergistic effect between the high active Fe_3O_4 nanoparticles and N-doped matrix endows this outstanding catalytic activity. The work presented here can be easily extended to prepare metal compounds decorated carbon nanomaterials with special structure for a broad range of energy storage and conversion devices.

KEYWORDS

oxygen reduction reaction, Zn-air battery, Fe_3O_4, N doping, hollow microsphere

1 Introduction

Oxygen reduction reaction (ORR) is a crucial reaction in clean energy storage and conversion devices such as fuel cells and metal-air batteries [1–3]. Up to now, Pt-based catalysts are still the most active and widespread utilized catalysts to accelerate the ORR rate [4, 5]. Therefore, the large-scale commercialization of these techniques was greatly restricted due to the high cost of Pt. And considerable efforts have been devoted to develop highly efficient and low-cost ORR catalysts including nonprecious metal and metal-free catalysts [6–8]. Regarding nonprecious metal catalysts, various metal oxides/sulfides/carbides/nitrides were extensively investigated and great progress was made [9–14]. However, their performance is still not comparable to Pt/C catalysts, and this is largely due to their poor conductivity [15]. Fortunately, carbon-based catalysts, one of the most important metal-free catalysts, possess very high conductivity, which can facilitate electron transfer during ORR [16–18]. What's more, the catalytic activity of carbon catalysts can be further improved by doping heteroatoms such as N, S, P et al. to modify their electronic and geometric effects [19–23]. Therefore, the combination of heteroatom doped carbon and nonprecious metal catalysts seems easier to achieve Pt-like catalytic activity.

On the other hand, for ORR, which taken place on the interface of catalysts and electrolyte, the exposure of more active sites of catalysts is very important. Therefore, reasonable designing the structure of ORR catalysts is essential. For this purpose, various structures such as hollow, core/shell and mesoporous were developed [24–27]. Hollow structures, which can not only increase exposed active sites, but also facilitate mass transport in ORR are very attractive. However, synthesis of hollow-structured catalysts usually involves the usage of complex hard-template method such as silica colloid, ordered mesoporous silica [28–30]. And the removal of hard-template will certainly complicate the process. Moreover, the surface of the catalysts synthesized via traditional template method is usually smooth, either prepared by sol-gel method or templated method [24, 31, 32]. If the surface of the catalysts is composed of 2D nanoplate, the mass transport in the catalysts and exposed active sites of the catalysts can be significantly increased.

Recently, it is proposed that Zn compounds such as ZnO can be used as template to synthesis porous carbon [33–35]. At high temperature, the ZnO will be reduced to Zn by carbon and Zn can evaporate off at approach its boiling point. The evaporation of Zn can lead to high surface area carbon like the $ZnCl_2$ activation mechanism [36, 37]. Moreover, compared with other hard-template, the utilization of volatile Zn-based template could also avoid the complex washing process. This strategy was also used when carbonizing Zn-based metal organic frameworks (MOFs) [38–40]. For example, by carbonizing Zn-based MOF, porous carbon materials

Address correspondence to Yanqiang Li, yanqiangli@dlut.edu.cn; Tingli Ma, tinglima@dlut.edu.cn; Siru Chen, siruchen@zut.edu.cn

with surface area as high as 3,405 $m^2 \cdot g^{-1}$ can be achieved [41]. What's more, the organic ligands that could complex with Zn usually can also complex with other transition metal such as Fe, Co, Ni, and create extra active sites after carbonization [42–44]. However, it is difficult to synthesis hollow MOFs via traditional hydrothermal or solvothermal method, and the exposed active site is limited.

Herein, we report a facile method to synthesis hollow carbon sphere encapsulated with Fe_3O_4 nanoparticles as highly efficient electrocatalyst for ORR. By using solid ZnO nanowires as Zn source, $FeCl_3$ as Fe source and 2-aminoterephthalic acid as ligand, hollow metal complex nanosphere composed of 2D nanoplate can be synthesized. After thermal annealing in nitrogen, the hollow metal complex nanosphere was carbonized to N doped hollow carbon sphere, and the Fe species can be transferred to high active Fe_3O_4 nanoparticles. Even though the Fe content is only as low as 0.56%, the catalyst could still achieve high ORR performance in terms of more positive half-wave potential compared with commercial 20 wt.% Pt/C catalyst. In addition, the catalyst also shows much better durability and methanol tolerance. We demonstrated that the N doped carbon are primary composition of the catalysts, high active and uniform distributed Fe_3O_4 nanoparticles provide extra active sites, and the hollow structure composed of 2D nanoplate further improves its catalytic activity.

2 Experimental

2.1 Preparation of metal complex nanospheres

Uniform ZnO nanowire and 2-aminoterephthalic acid were used to synthesis the metal complex nanospheres. In a typical procedure, 0.082 g of ZnO nanowire and 0.182 g of 2-aminoterephthalic acid were dispersed in 36 mL DMF and 12 mL H_2O. After stirring for 10 min, the mixture was aged at 30 °C for 3 days. Then the obtained white powder was collected by centrifugation and washed with DMF and ethanol for several times, and dried at 60 °C for 12 h. The obtained sample was denoted as Zn-complex. The ZnFe-complex was synthesized with the same procedure except that a certain amount (100, 200, and 300 μL) of $FeCl_3$ solution (0.04 M) was added in the above mixture solution. The obtained samples were denoted as ZnFe@complex-1, ZnFe@complex-2 and ZnFe@complex-3, respectively.

2.2 Preparation of N doped hollow carbon sphere (NHCS) and Fe_3O_4@NHCSs

The NHCSs and Fe_3O_4@NHCSs were obtained by thermal annealing the corresponding metal complex at 900 °C for 2 h with a ramping rate of 5 °C·min^{-1} under argon. For example, the catalyst derived from Zn-complex are denoted as NHCS. And the catalysts derived from ZnFe-complex-*x* are named as Fe_3O_4@NHCS-*x*.

2.3 Characterization

The X-ray diffraction (XRD) patterns were recorded with a Riguku D/MAX2550 diffractometer. Renishaw inVia Raman spectrometer with an Ar ion laser as the excitation source was used to measure the Raman spectra. X-ray photoelectron spectroscopy (XPS) spectra were measured using ESCALAB 250Xi (ThermoFisher). Field emission scanning electron microscopy (FE-SEM) measurement was performed using Nova NanoSEM 450 (FEI) instrument. The transmission electron microscopy (TEM) and high-resolution transmission electron microscopy (HRTEM) images were obtained in FEI Tecnai G2 F20 S-TWIN electron microscope at an accelerating voltage of 200 kV. Nitrogen adsorption/desorption data were collected by Autosorb-iQ2 (Quantachrome Instruments) at 77 K. The specific surface area was calculated based on Brunauer–Emmett–Teller (BET) method and the pore size distribution curve was calculated by quenched solid density functional theory (QSDFT).

2.4 Electrochemical measurements

The electrochemical measurements were performed in a three-electrode system using CHI 760E potentiostat workstation. A platinum wire and an Ag/AgCl electrode were used as the counter electrode and reference electrode. The working electrode was a 5 mm (diameter) glassy carbon disk and the catalyst loading amount on the electrode was 0.2 mg·cm^{-2}. The electrolyte was 0.1 M KOH. Koutecky–Levich equations were used to determine the kinetics parameters

$$1/j = 1/j_k + 1/(B\omega^{1/2})$$

$$B = 0.2nFC_0(D_0)^{2/3}\nu^{-1/6}$$

where j is measured current, j_k is the kinetic current, ω is the electrode rotation rate in rpm. The constant 0.2 is feasible when the rotation rate is in rpm and F means the Faraday constant (96,485 C·mol^{-1}). n represents the electron transfer number per O_2. ν is the kinematic viscosity of the electrolyte (0.01 $cm^2 \cdot s^{-1}$), D_0 is the diffusion coefficient of O_2 (1.9×10^{-5} $cm^2 \cdot s^{-1}$), C_0 is the bulk concentration of O_2 (1.2×10^{-3} mol·L^{-1}).

The performance of Zn-air batteries was evaluated using a home-built electrochemical cells. Briefly, zinc foil was used as anode and catalysts loaded on the gas diffusion layer (Nafion-coated carbon cloth paper with a geometric area of 1.0 cm^2, catalyst loading amount of 1.0 mg·cm^{-2}) used as the air cathode. The electrolyte was 6.0 M KOH and 0.2 M zinc acetate solution. Polarization curves were obtained using the linear sweep voltammetry (LSV) technique with a CHI 760E electrochemical working station. The galvanostatic discharge and charge cycling (5 min discharge and 5 min charge with a current density of 10 mA·cm^{-2}) was performed in a LAND testing system. The specific capacitance of the Zn-air battery was calculated from the equation: $C_{sp} = i \times t/\Delta m$, where i is the discharge current, t is the discharge time and Δm is the weight of the consumed zinc.

3 Results and discussion

The illustration for the synthesis of the Fe_3O_4@NHCSs is shown in Scheme 1. First of all, uniform ZnO nanowire was prepared and used as Zn source to complex with 2-aminoterephthalic acid (Fig. S1 in the Electronic Supplementary Material (ESM)). From the TEM images of ZnO, we can clearly see the ZnO shows a rod-like morphology with a width of 50–100 nm. The lattice distance of 0.261 nm is the lattice fringes (002) of ZnO, indicating the successful preparation of ZnO nanowire (Fig. S2 in the ESM). After aging at room temperature for 3 days, the ZnO nanowire disappeared completely and spherical product was obtained after centrifugation. During the reaction process, $FeCl_3$ can be introduced owing to the fact that Fe^{3+} can also coordinate with 2-aminoterephthalic acid. The XRD pattern shown in Fig. S3 in the ESM demonstrated the formation of Zn-complex and ZnFe-complex. Due to the low iron content, the morphology of the ZnFe-complex and Zn-complex are the same. The morphology of the complex is shown in Fig. 1(a) and Fig. S4 in the ESM. It can be seen that the complex exhibits a uniform sphere morphology with an average diameter of 3 μm. In addition, the sphere is composed by 2D nanoplate. After thermal annealed at 900 °C for 2 h, the NHCS or Fe_3O_4@NHCSs were obtained. As shown in Fig. 1(b) and Fig. S5 in the ESM, we can see that thermal annealing process does not break the morphology of the sphere except a little shrinkage in size. And the uniform carbon sphere composed by 2D nanoplate was successfully prepared. From the enlarged SEM image, we can see that there are many pores on the nanoplate, indicating that the carbon sphere may possess very high surface area (Fig. S6 in the ESM). Moreover, the carbon sphere is hollow structure and this can be clearly seen from the crack

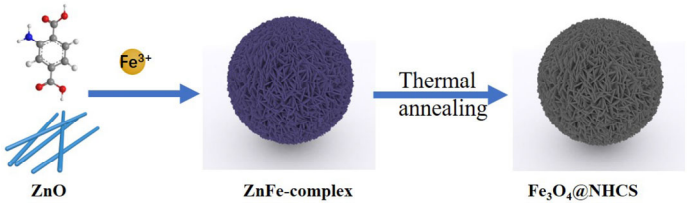

Scheme 1 Illustration of the preparation of Fe_3O_4/NHCS.

sphere in Fig. 1(b). The hollow structure is also demonstrated by TEM image, where clear contrast ratio was obviously in the centre and shell of the carbon sphere (Fig. 1(c)). The element mapping images indicate that Fe, N, C and O are distributed homogeneously in the carbon shell (Fig. 1(e)). However, for Zn element map, there is only a few scattered distributions other than sphere shape, which is very different from that of C, N, O and Fe, indicating that the Zn elemental is completely evaporated. To investigate the formation mechanism of the Zn-complex hollow sphere, soluble zinc salts such as $ZnCl_2$ or $Zn(NO_3)_2$ were used as zinc source during the synthesis process instead of ZnO nanowire. However, no any solid product was obtained. Thus, we infer that the solid zinc source is crucial. It is proposed that the –COOH group can react with ZnO in the solvent and release Zn^{2+} slowly, then the Zn^{2+} coordinates with the –COO– group slowly to assemble the microsphere. To further confirm the advantage of ZnO nanowire, ZnO nanosphere was used as Zn source to synthesize the complex. Though 2D nanoplate assembled sphere can be obtained. However, the sphere is not hollow structure. Moreover, after calcinating at high temperature, the sphere tends to collapse and the nanoplate stacks with each other (Fig. S7 in the ESM). Thus, the solid ZnO nanowire as zinc source is crucial to obtain the special hollow microsphere.

XRD was used to identify the composite of NHCS and Fe_3O_4@NHCSs (Fig. 2(a)). Two board peaks centred at 24° and 44° are observed for all the samples, which are corresponding to the (002) and (100) planes of the graphite carbon, demonstrating the formation of carbon structure. However, for Fe_3O_4@NHCSs, besides to the carbon peaks, typical peaks corresponding to Fe_3O_4 (PDF No. 75-0033) are also observed, indicating that the iron is converted into Fe_3O_4 during the thermal annealing process. With the increasing of iron in the synthesis process, the peaks of Fe_3O_4 become stronger. The HRTEM image shown in Fig. 1(d) also demonstrated the formation of Fe_3O_4. The lattice distance of 0.482 nm is the lattice fringes (111) of Fe_3O_4. The bulk mass percentages of iron in the Fe_3O_4/NHCSs were examined by inductively coupled plasma optical emission spectroscopy (ICP-OES) analysis, and the iron content was determined to be 0.41 wt.%, 0.56 wt.% and 0.88 wt.% in Fe_3O_4@NHCSs-1, Fe_3O_4@NHCSs-2 and Fe_3O_4@NHCSs-3, respectively.

It should be noted that no peaks related to Zn can be observed, indicating that there is no Zn element in the samples. This can be attributed to the low boiling point of Zn and long-time thermal annealing, which is usually observed in carbonizing of Zn-containing MOFs. In the thermal annealing process, the Zn-based compound was reduced to Zn by the carbon and evaporated off. Raman spectra also indicated the formation of carbon, where two sharp peaks at around 1,360 (D band) and 1,580 cm^{-1} (G band) are observed, corresponding to the disordered carbon and graphitic sp^2 hybridized carbon, respectively. The intensity ratio of the D band to G band (I_D/I_G) can be used to investigate the defects of carbon. It can be seen from Fig. 2(b) that this value increased with the increasing of Fe_3O_4 content, indicating that the Fe_3O_4 is incorporated into the carbon and induces more defects accordingly.

XPS measurements are performed to gain the detailed chemical composition and bonding configuration of Fe_3O_4/NHCS-2. From the survey spectra in Fig. S8 in the ESM, characteristic peaks related to C, N, O and Fe can be observed at 284, 400, 532 and 711 eV, though the signal of Fe is not very obvious due to its low content. The N content is estimated to be 4.23% according to the XPS result. The N content for other samples is also measured and listed in Table S1 in the ESM. It is interesting that the N content increased with the increasing of iron in the samples, indicating that there may be an interaction between the Fe and N species. The interaction between Fe and N is demonstrated by the positive shift of N 1s peak from NHCS to Fe_3O_4/NHCS-2 (Fig. S9 in the ESM). The high resolution N 1s spectra can be deconvoluted into three peaks at 398.8, 400.5 and 401.2 eV, corresponding to the pyridinic N, pyrrolic N and graphitic N (Fig. 2(c)) [45, 46]. The relative percentages and content of the different N species are also calculated according to their integrated area for NHCS and Fe_3O_4@NHCS-2. The pyridinic N, pyrrolic N and graphitic N are 11.22%. 33.41% and 55.37% for NHCS and these values are 9.73%, 42.90% and 47.37% for Fe_3O_4@NHCS-2. Obvious, the content of pyridinic-N and pyrrolic-N increased in Fe_3O_4@NHCS-2. This is due to the fact that pyridinic-N and pyrrolic-N are responsible for the formation of metal–nitrogen sites. Five peaks at the high-resolution Fe 2p spectrum can be observed (710.9, 714, 718.7, 724.1 and 726.2 eV), once again demonstrating the existence of Fe_3O_4 (Fig. 2(d)) [47, 48]. The peaks at 711 and 714 eV can be assigned to the $2p_{3/2}$ of the Fe(III) and Fe(II) ions, respectively. The peak at 726.2 eV is attributed to the binding energies of $2p_{1/2}$ of Fe(III) and Fe(II) ions, and the peaks at 724.1 eV can be assigned to the binding energies of $2p_{1/2}$ of Fe(II) ion [49, 50]. The peak at 718.7 eV is a satellite peak for the above four peaks, demonstrating that Fe mainly exists in ionic state and the co-existence of Fe(III) and Fe(II).

The pore structures of the catalysts are analysed by N_2

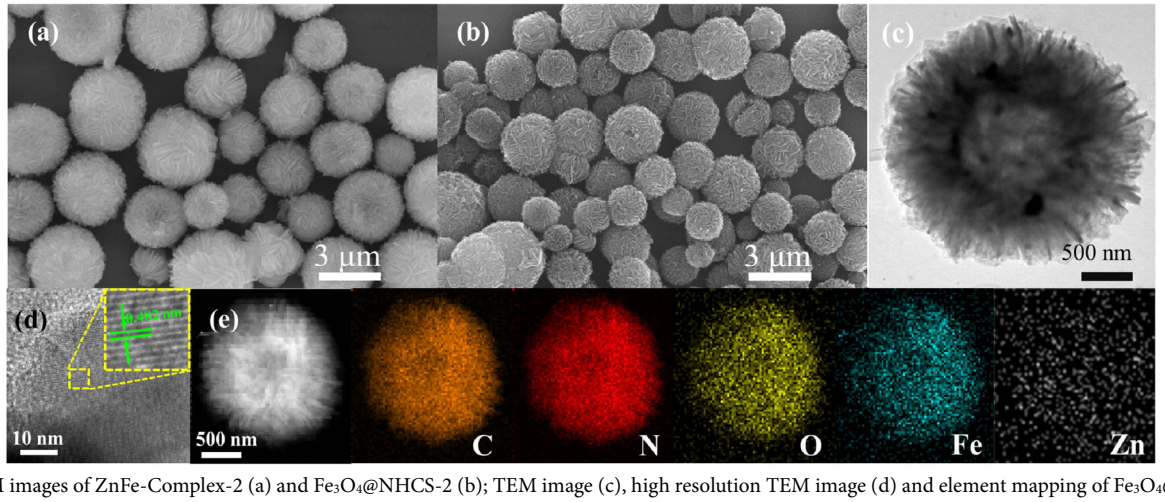

Figure 1 SEM images of ZnFe-Complex-2 (a) and Fe_3O_4@NHCS-2 (b); TEM image (c), high resolution TEM image (d) and element mapping of Fe_3O_4@NHCS-2 (e).

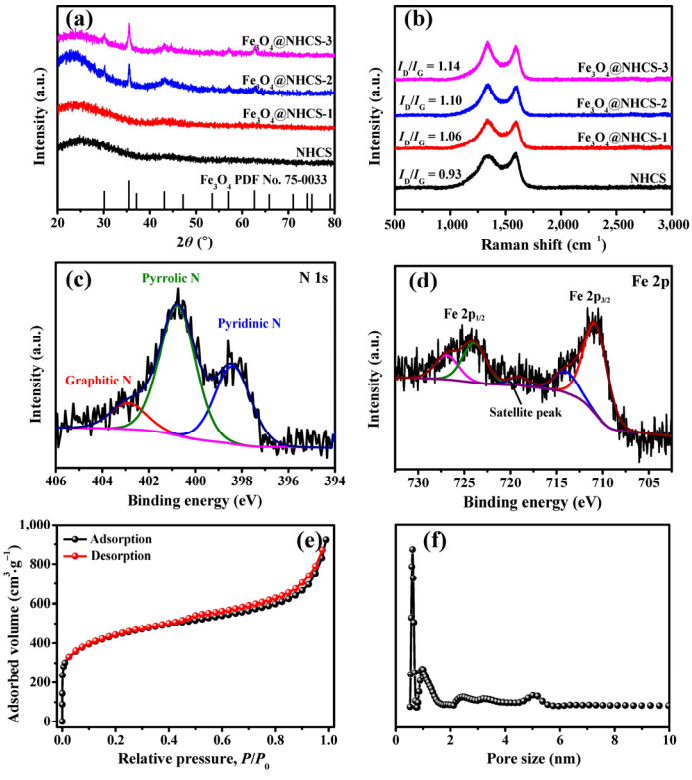

Figure 2 XRD patterns (a) and Raman spectra (b) of NHCS, Fe_3O_4@NHCS-1, Fe_3O_4@NHCS-2 and Fe_3O_4@NHCS-3. High-resolution N 1s (c) and Fe 2p (d) XPS spectra of for Fe_3O_4@NHCS-2. Adsorption/desorption (e) and pore size distribution (f) curves of Fe_3O_4@NHCS-2.

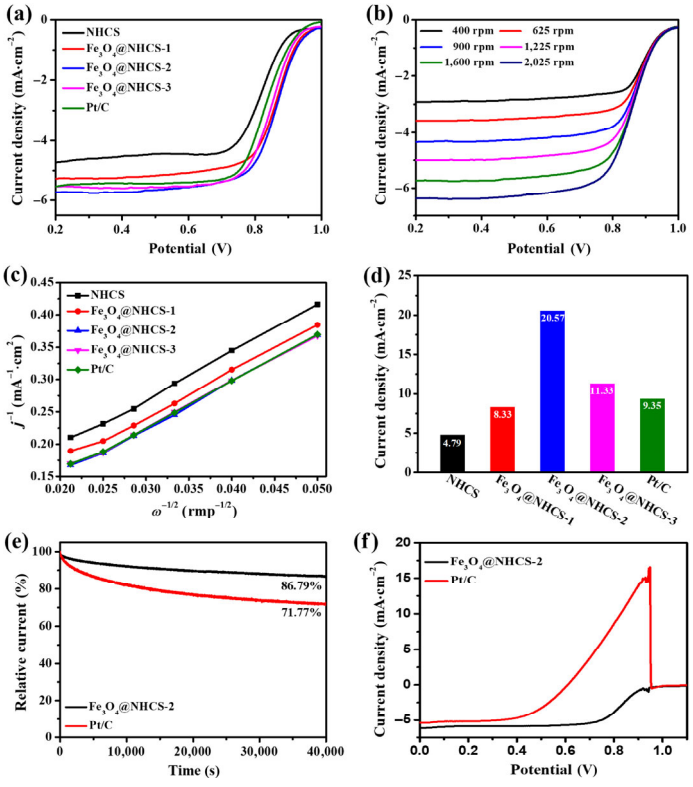

Figure 3 (a) RDE polarization curves of NHCS, Fe_3O_4@NHCS-1, Fe_3O_4@NHCS-2, Fe_3O_4@NHCS-3 and Pt/C. (b) RDE polarization curves of Fe_3O_4@NHCS-2 at different rotating speeds. (c) K-L plots of NHCS, Fe_3O_4@NHCS-1, Fe_3O_4@NHCS-2, Fe_3O_4@NHCS-3 and Pt/C at 0.7 V. (d) The kinetic current density of NHCS, Fe_3O_4@NHCS-1, Fe_3O_4@NHCS-2, Fe_3O_4@NHCS-3 and Pt/C at 0.8 V. (e) Chronoamperometric curves of Fe_3O_4@NHCS-2 and Pt/C for 40,000 s. (f) LSV curves of Fe_3O_4@NHCS-2 and Pt/C electrodes upon the addition of 3 M methanol (20 mL) to the electrolyte (180 mL).

adsorption–desorption measurements (Fig. 2(e) and Fig. S10 in the ESM). All the samples exhibit typical type-I isotherms with a sharp increase at the low-pressure range, indicating the presence of plenty of micropores. The BET specific surface area of NHCS is as high as 1,819 $m^2 \cdot g^{-1}$, surpassing most of the reported carbon sphere catalyst [51, 52]. The high surface area can be attributed to the evaporation of Zn species during the thermal annealing process. After incorporation of Fe_3O_4, the specific surface area of Fe_3O_4@NHCSs decreased little, but is still in the range of 1,453–1,675 $m^2 \cdot g^{-1}$ (Table S1 in the ESM). The pore-size distribution curve also demonstrates the microspore structure, where pores mainly located at 0.6 and 1.0 nm are observed. Obviously, the highly porous structure of the carbon will benefit its catalytic activity. In addition, the hierarchical 3D sphere structure assembled by 2D nanoplate will certainly in favor of mass transport and the exposure of active sites, due to the more exposed surface area, thus the catalytic activity of the catalysts is expected to be very attractive.

The catalytic activity of the catalysts toward ORR was examined by a pine rotating disk electrode device connected to CHI 760E potentiostat workstation. As depicted in Fig. S11 in the ESM, there is only double-layer charging current in N_2-saturated 0.1 $mol \cdot L^{-1}$ KOH for Fe_3O_4@NHCSs-2, while an obvious cathodic peak was clearly observed in O_2-saturated electrolyte, suggesting its potential for ORR. In addition, it can be seen that the cathodic peak shift positively from NHCS to Fe_3O_4@NHCSs, indicating that the introduction of Fe_3O_4 can boost the catalytic activity of the carbon sphere. This phenomenon was further demonstrated by the LSV curves. It can be seen from Fig. 3(a) that NHCS exhibits the worst ORR performance with an onset potential of 0.952 V (defined as the corresponding potential when reaching an ORR current density of 0.3 $mA \cdot cm^{-2}$), and a half-wave potential of 0.822 V. While for Fe_3O_4@NHCSs, the ORR activities increase greatly. In fact, the performance of all the Fe_3O_4@NHCSs surpasses commercial 20 wt.% Pt/C in terms of onset potential and half-wave potential (Table S2 in the ESM). Especially for Fe_3O_4@NHCS-2, its half-wave potential is 25 mV higher than that of Pt/C. The results also indicate that proper Fe_3O_4 amount is important for the catalytic activity not only relays on the number of active sites, but also depends on the catalysts' structure such as surface area. In general, higher surface area usually means more exposed active. That's, the effective active site is important. From Table S1 in the ESM, we can see that the surface area of the Fe_3O_4@NHCSs exhibits a decrease trend with the increasing of Fe_3O_4 content. Fe_3O_4@NHCS-2, which possesses high surface area and enough active site, exhibits highest ORR activity. Another reason for the high ORR performance of the catalysts is their hollow structure. As shown above, when ZnO nanosphere was used to synthesize the catalyst, nanoplate assembled sphere without hollow structure was achieved. However, the catalytic activity of the non-hollow catalyst is rather poor (Fig. S12 in the ESM). Thus, the high catalytic activity of Fe_3O_4@NHCS-2 can be attributed to its unique structure and high active Fe_3O_4 species.

Rotating disk electrode (RDE) measurements were conducted at different rotating speeds to further investigate the catalyst kinetics of the catalysts (Fig. 3(b) and Fig. S13 in the ESM). The diffusion current densities increased with the increasing of rotating speed, and this can be attributed to the shortened O_2 diffusion distance at high rotation speed. The linear K-L plots indicate first-order reaction kinetics toward the concentration of dissolved O_2 (Fig. 3(c)). The electron transfer numbers calculated at 0.7 V from the slopes of K-L plots are 3.85, 3.95, 4.02 and 3.99 for NHCS, Fe_3O_4@NHCS-1, Fe_3O_4@NHCS-2, and Fe_3O_4@NHCS-3, suggesting that each catalyst follows a four- electron transfer process. The kinetic limiting current densities (J_k) of the catalysts are calculated from the intercepts of the K-L plots to better compare the catalytic activity of the catalysts.

The J_k describes the real kinetics of an electrocatalytic reaction and is directly related to the activity of an electrocatalyst. Impressively, Fe_3O_4@NHCS-2 shows the highest J_k value of 20.57 mA·cm^{-2}, much higher than those for NHCS (4.79 mA·cm^{-2}) Fe_3O_4@NHCS-1 (8.33 mA·cm^{-2}), Fe_3O_4@NHCS-3 (11.31 mA·cm^{-2}) and Pt/C (9.35 mA·cm^{-2}), demonstrating its superior ORR activity (Fig. 3(d)).

Chronoamperometric measurements was conducted at 0.3 V to evaluate the durability of Fe_3O_4@NHCS-2 and Pt/C. In contrast to Pt/C catalyst, when 71.77% current density was maintained after 40,000 s, Fe_3O_4@NHCS-2 exhibits much higher stability (86.79% current density can be maintained), suggesting the superiority in practical application (Fig. 3(e)). In addition, Fe_3O_4@NHCS-2 exhibits high tolerance to methanol. As shown in Fig. 3(f), after pouring 3 M methanol into the KOH electrolyte, the LSV curve of Fe_3O_4@NHCS-2 remains the same, while a sharp methanol oxidation peak was observed for Pt/C. The remarkable catalytic activity as well as stability and excellent methanol resistance of the Fe_3O_4/NHCS-2 makes it a promising alternative for the ORR electrocatalysts.

Besides ORR, the oxygen evolution reaction (OER) performance of the catalysts is also investigated. As shown in Fig. S14 in the ESM. It can be seen the OER activity of NHCS is also the worst, and the introduction of Fe_3O_4 can obviously improve the OER activity of the catalysts. In addition, with the increasing of Fe_3O_4 content in the NHCS, the OER performance of the catalysts increases, highlighting the importance of Fe_3O_4. To deliver a current density of 10 mA·cm^{-2}, NHCS needs a potential of 1.69 V (460 mV overpotential), and these values are 1.67 V (440 mV overpotential), 1.64 V (420 mV overpotential), and 1.62 V (390 mV overpotential) for Fe_3O_4@NHCS-1, Fe_3O_4@NHCS-2 and Fe_3O_4@NHCS-3. The reversible oxygen electrode property can be assessed by the variance of OER and ORR metrics ($\Delta E = E_{j=10} - E_{1/2}$, where $E_{j=10}$ is the operating potential at 10 mA·cm^{-2} for OER, while $E_{1/2}$ is the half-wave potential for ORR). Impressively, Fe_3O_4@NHCS-2 and Fe_3O_4@NHCS-3 exhibit similar ΔE (0.78 and 0.77 V), much smaller than that for NHCS (0.87 V), once again demonstrating the advantage of Fe_3O_4 species.

The excellent catalytic activity of Fe_3O_4@NHCS-2 inspired us to build a home-made Zn-air battery to evaluate its practical application. The test was conducted in ambient conditions without external gas purging. The open-circuit voltage was determined to be as high as 1.42 V and two primary Zn-air batteries connected in series could easily power a red light-emitting diode (LED), demonstrating its promising application in Zn-air batteries (Figs. 4(a) and 4(b)). In addition, the maximum power density was calculated as 133 mW·cm^{-2}, which is even higher than that of 20 wt.% Pt/C (115 mW·cm^{-2}) (Fig. 4(c)). It also should be noted that the high-power density is comparable to other state-of-the-art electrode materials (Table S3 in the ESM). When galvanostatically discharged at 10.0 mA cm^{-2}, the Zn-air battery delivers a stable discharge voltage around 1.12 V with only little degradation. Furthermore, it yields a specific capacity of 701 mA·h·g^{-1} normalized to the mass of consumed Zn and this value is 665 mA·h·g^{-1} for Pt/C catalysts at the same condition (Fig. 4(d)). Obviously, the larger power and energy densities suggest that Fe_3O_4@NHCS-2 could serve as the low-cost catalyst in Zn-air batteries. For rechargeable Zn-air batteries, the charge process of the catalyst is also very important. Thus, the charge curves of Fe_3O_4@NHCS-2 for Zn-air batteries were also measured, and commercial Pt/C+IrO_2 with a mass of 1:1 was used for comparison. Due to the relatively poor OER activity of Fe_3O_4@NHCS-2, the charging process of Fe_3O_4@NHCS-2 is a little worse than Pt/C+IrO_2. However, the discharging process of Fe_3O_4@NHCS-2 is obviously better than the Pt/C+IrO_2 (Fig. S15 in the ESM). Moreover, the long-time cycling ability of Fe_3O_4@NHCS-2 is also very good. As shown in Fig. 4(e), the Zn-air battery based on Fe_3O_4@NHCS-2 catalyst delivers an initial discharge potential of 1.12 V and a charge potential of 2.30 V (52.6% energy efficiency). After 50 h cycling, the discharge potential and charge potential are 1.12 and 2.45 V, that the energy efficiency is still 45.7%. By contrast, for Pt/C, the energy efficiency after 50 h cycling is only 39.6% (2.55 V for charging and 1.01 V for discharging), much lower than that of Fe_3O_4@NHCS-2. The outstanding discharging behaviour and durable stability of Zn-air battery based on Fe_3O_4@NHCS-2 once again imply its potential applications.

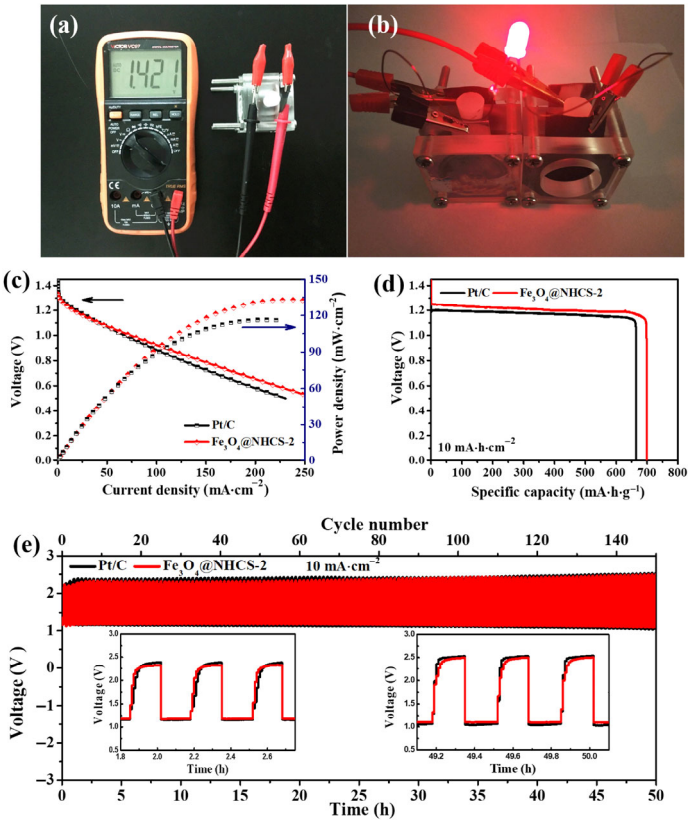

Figure 4 (a) Photograph of the assembled battery with an open-circuit voltage of 1.42 V. (b) Digital images of LEDs (2.2 V) after being powered by two Zn-air batteries (catalyzed by Fe_3O_4@NHCS-2) in series. (c) Polarization and power density curves of primary Zn-air batteries using Fe_3O_4@NHCS-2 and Pt/C as ORR catalyst. (d) Discharge curves of Zn-air batteries assembled from Fe_3O_4@NHCS-2 and Pt/C catalysts at 10.0 mA·cm^{-2} discharging rate. (e) Long time cycling test of Fe_3O_4@NHCS-2 and Pt/C at 10.0 mA·cm^{-2}.

4 Conclusions

In conclusion, we propose a facile approach to prepare Fe_3O_4 decorated N doped hollow carbon microsphere from ZnFe-complex. In addition, the hollow microsphere is assembled by 2D nanoplate and this guarantees more exposed catalytic active sites. The usage of solid ZnO nanowire as zinc source is crucial to obtain this structure. The optimized sample Fe_3O_4@NHCS-2 shows superior ORR performance compared with commercial Pt/C in 0.1 M KOH solution. Remarkably, the Fe_3O_4@NHCS-2 also confers excellent Zn-air battery performance with a high-power density of 133 mW·cm^{-2} and high specific capacity of 701 mA·h·g^{-1}, as well as high energy efficiency and excellent long-time durability. The outstanding ORR performance can be attributed to its high surface with hollow structure that facilitates fast transport of reactants and electrolytes toward the active sites, the high active Fe_3O_4 species and the N doped carbon matrix. Moreover, the synthetic method presented can be easily extended to prepare other nonprecious metal compounds decorated carbon material for various energy conversion and storage technologies.

Acknowledgements

This work is supported by the National Natural Science Foundation

of China (No. 51772039), the Fundamental Research Funds for the Central University (No. DUT18LK13). The Research Center for Solar Light Energy Conversion, Kyushu Institute of Technology, Japan also supports this work financially.

Electronic Supplementary Material: Supplementary material (SEM and TEM images of the ZnO nanowire, the ZnFe-complex and the catalysts, and LSV curves, XPS spectra and N_2 adsorption curves of the catalysts) is available in the online version of this article at https://doi.org/10.1007/s12274-019-2512-7.

References

[1] Debe, M. K. Electrocatalyst approaches and challenges for automotive fuel cells. *Nature* **2012**, *486*, 43–51.

[2] Wang, T. T.; Wu, J. H.; Liu, Y. L.; Cui, X.; Ding, P.; Deng, J.; Zha, C. Y.; Coy, E.; Li, Y. G. Scalable preparation and stabilization of atomic-thick CoNi layered double hydroxide nanosheets for bifunctional oxygen electrocatalysis and rechargeable zinc-air batteries. *Energy Storage Mater*. **2019**, *16*, 24–30.

[3] Fu, S. F.; Zhu, C. Z.; Song, J. H.; Du, D.; Lin, Y. H. Metal-organic framework-derived non-precious metal nanocatalysts for oxygen reduction reaction. *Adv. Energy Mater*. **2017**, *7*, 1700363.

[4] Wang, D. L.; Xin, H. L.; Hovden, R.; Wang, H. S.; Yu, Y. C.; Muller, D. A.; DiSalvo, F. J.; Abruña, H. D. Structurally ordered intermetallic platinum-cobalt core-shell nanoparticles with enhanced activity and stability as oxygen reduction electrocatalysts. *Nat. Mater*. **2013**, *12*, 81–87.

[5] Wang, N.; Li, L. G.; Zhao, D. K.; Kang, X. W.; Tang, Z. H.; Chen, S. W. Graphene composites with cobalt sulfide: Efficient trifunctional electrocatalysts for oxygen reversible catalysis and hydrogen production in the same electrolyte. *Small* **2017**, *13*, 1701025.

[6] Dai, L. M.; Xue, Y. H.; Qu, L. T.; Choi, H. J.; Baek, J. B. Metal-free catalysts for oxygen reduction reaction. *Chem. Rev*. **2015**, *115*, 4823–4892.

[7] Tian, H.; Wang, N.; Xu, F. G.; Zhang, P. F.; Hou, D.; Mai, Y. Y.; Feng, X. L. Nitrogen-doped carbon nanosheets and nanoflowers with holey mesopores for efficient oxygen reduction catalysis. *J. Mater. Chem. A* **2018**, *6*, 10354–10360.

[8] Amiinu, I. S.; Liu, X. B.; Pu, Z. H.; Li, W. Q.; Li, Q. D.; Zhang, J.; Tang, H. L.; Zhang, H. N.; Mu, S. C. From 3D ZIF nanocrystals to Co-N_x/C nanorod array electrocatalysts for ORR, OER, and Zn-air batteries. *Adv. Funct. Mater*. **2018**, *28*, 1704638.

[9] Wang, R.; Dong, X. Y.; Du, J.; Zhao, J. Y.; Zang, S. Q. MOF-derived bifunctional Cu_3P nanoparticles coated by a N, P-codoped carbon shell for hydrogen evolution and oxygen reduction. *Adv. Mater*. **2018**, *30*, 1703711.

[10] Tang, F.; Lei, H. T.; Wang, S. J.; Wang, H. X.; Jin, Z. X. A novel Fe-N-C catalyst for efficient oxygen reduction reaction based on polydopamine nanotubes. *Nanoscale* **2017**, *9*, 17364–17370.

[11] Hu, Y.; Jensen, J. O.; Zhang, W.; Cleemann, L. N.; Xing, W.; Bjerrum, N. J.; Li, Q. F. Hollow spheres of iron carbide nanoparticles encased in graphitic layers as oxygen reduction catalysts. *Angew. Chem., Int. Ed*. **2014**, *53*, 3675–3679.

[12] Xia, W.; Mahmood, A.; Liang, Z. B.; Zou, R. Q.; Guo, S. J. Earth-abundant nanomaterials for oxygen reduction. *Angew. Chem., Int. Ed*. **2016**, *55*, 2650–2676.

[13] Qiao, Y. Y.; Yuan, P. F.; Hu, Y. F.; Zhang, J. N.; Mu, S. C.; Zhou, J. H.; Li, H.; Xia, H. C.; He, J.; Xu, Q. Sulfuration of an Fe-N-C catalyst containing Fe_xC/Fe species to enhance the catalysis of oxygen reduction in acidic media and for use in flexible Zn-air batteries. *Adv. Mater.* **2018**, *30*, 1804504.

[14] Guo, Y. Y.; Yuan, P. F.; Zhang, J. N.; Hu, Y. F.; Amiinu, I. S.; Wang, X.; Zhou, J. G.; Xia, H. C.; Song, Z. B.; Xu, Q. et al. Carbon nanosheets containing discrete Co-N_x-B_y-C active sites for efficient oxygen electrocatalysis and rechargeable Zn-air batteries. *ACS Nano* **2018**, *12*, 1894–1901.

[15] Han, C.; Li, Q.; Wang, D. W.; Lu, Q. Q.; Xing, Z. C.; Yang, X. R. Cobalt sulfide nanowires core encapsulated by a N, S codoped graphitic carbon shell for efficient oxygen reduction reaction. *Small* **2018**, *14*, 1703642.

[16] Luo, H.; Jiang, W. J.; Zhang, Y.; Niu, S.; Tang, T.; Huang, L. B.; Chen, Y. Y.; Wei, Z. D.; Hu, J. S. Self-terminated activation for high-yield production of N, P-codoped nanoporous carbon as an efficient metal-free electrocatalyst for Zn-air battery. *Carbon* **2018**, *128*, 97–105.

[17] Chai, G. L.; Qiu, K.; Qiao, M.; Titirici, M. M.; Shang, C. X.; Guo, Z. X. Active sites engineering leads to exceptional ORR and OER bifunctionality in P, N co-doped graphene frameworks. *Energy Environ. Sci*. **2017**, *10*, 1186–1195.

[18] Chen, P. Z.; Zhou, T. P.; Xing, L. L.; Xu, K.; Tong, Y.; Xie, H.; Zhang, L. D.; Yan, W. S.; Chu, W. S.; Wu, C. Z. et al. Atomically dispersed iron-nitrogen species as electrocatalysts for bifunctional oxygen evolution and reduction reactions. *Angew. Chem., Int. Ed*. **2017**, *56*, 610–614.

[19] Borghei, M.; Laocharoen, N.; Kibena-Põldsepp, E.; Johansson, L. S.; Campbell, J.; Kauppinen, E.; Tammeveski, K.; Rojas, O. J. Porous N, P-doped carbon from coconut shells with high electrocatalytic activity for oxygen reduction: Alternative to Pt-C for alkaline fuel cells. *Appl. Catal. B: Environ*. **2017**, *204*, 394–402.

[20] Zheng, X. J.; Wu, J.; Cao, X. C.; Abbott, J.; Jin, C.; Wang, H. B.; Strasser, P.; Yang, R. Z.; Chen, X.; Wu, G. N-, P-, and S-doped graphene-like carbon catalysts derived from onium salts with enhanced oxygen chemisorption for Zn-air battery cathodes. *Appl. Catal. B: Environ*. **2019**, *241*, 442–451.

[21] Li, Y. Q.; Xu, H. B.; Huang, H. Y.; Gao, L. G.; Zhao, Y. Y.; Ma, T. L. Facile synthesis of N, S co-doped porous carbons from a dual-ligand metal organic framework for high performance oxygen reduction reaction catalysts. *Electrochim. Acta* **2017**, *254*, 148–154.

[22] Niu, W. H.; Li, L. G.; Liu, X. J.; Wang, N.; Liu, J.; Zhou, W. J.; Tang, Z. H.; Chen, S. W. Mesoporous N-doped carbons prepared with thermally removable nanoparticle templates: An efficient electrocatalyst for oxygen reduction reaction. *J. Am. Chem. Soc*. **2015**, *137*, 5555–5562.

[23] Hua, Y. Q.; Jiang, T. T.; Wang, K.; Wu, M. M.; Song, S. Q.; Wang, Y.; Tsiakaras, P. Efficient Pt-free electrocatalyst for oxygen reduction reaction: Highly ordered mesoporous N and S co-doped carbon with saccharin as single-source molecular precursor. *Appl. Catal. B: Environ*. **2016**, *194*, 202–208.

[24] Wang, H. T.; Wang, W.; Xu, Y. Y.; Dong, S.; Xiao, J. W.; Wang, F.; Liu, H. F.; Xia, B. Y. Hollow nitrogen-doped carbon spheres with Fe_3O_4 nanoparticles encapsulated as a highly active oxygen-reduction catalyst. *ACS Appl. Mater. Interfaces* **2017**, *9*, 10610–10617.

[25] Wang, Y.; Liu, H. Y.; Wang, K.; Song, S. Q.; Tsiakaras, P. 3D interconnected hierarchically porous N-doped carbon with NH_3 activation for efficient oxygen reduction reaction. *Appl. Catal. B: Environ*. **2017**, *210*, 57–66.

[26] Park, J.; Kwon, T.; Kim, J.; Jin, H.; Kim, H. Y.; Kim, B.; Joo, S. H.; Lee, K. Hollow nanoparticles as emerging electrocatalysts for renewable energy conversion reactions. *Chem. Soc. Rev*. **2018**, *47*, 8173–8202.

[27] Pei, Y. C.; Qi, Z. Y.; Li, X. L.; Maligal-Ganesh, R. V.; Goh, T. W.; Xiao, C. X.; Wang, T. Y.; Huang, W. Y. Morphology inherence from hollow MOFs to hollow carbon polyhedrons in preparing carbon-based electrocatalysts. *J. Mater. Chem. A* **2017**, *5*, 6186–6192.

[28] Liang, H. W.; Wei, W.; Wu, Z. S.; Feng, X. L.; Müllen, K. Mesoporous metal-nitrogen-doped carbon electrocatalysts for highly efficient oxygen reduction reaction. *J. Am. Chem. Soc*. **2013**, *135*, 16002–16005.

[29] Gao, S. Y.; Fan, B. F.; Feng, R.; Ye, C. L.; Wei, X. J.; Liu, J.; Bu, X. H. N-doped-carbon-coated Fe_3O_4 from metal-organic framework as efficient electrocatalyst for ORR. *Nano Energy* **2017**, *40*, 462–470.

[30] Singh, D. K.; Jenjeti, R. N.; Sampath, S.; Eswaramoorthy, M. Two in one: N-doped tubular carbon nanostructure as an efficient metal-free dual electrocatalyst for hydrogen evolution and oxygen reduction reactions. *J. Mater. Chem. A* **2017**, *5*, 6025–6031.

[31] Li, X. C.; Zhang, L.; He, G. H. Fe_3O_4 doped double-shelled hollow carbon spheres with hierarchical pore network for durable high-performance supercapacitor. *Carbon* **2016**, *99*, 514–522.

[32] Huang, J.; Cheng, S. P.; Chen, Y. X.; Chen, Z. L.; Luo, H.; Xia, X. H.; Liu, H. B. High-rate capability and long-term cycling of self-assembled hierarchical Fe_3O_4/carbon hollow spheres through interfacial control. *J. Mater. Chem. A* **2019**, *7*, 16720–16727.

[33] Li, Y. Q.; Huang, H. Y.; Chen, S. R.; Wang, C.; Ma, T. L. Nanowire-templated synthesis of FeN_x-decorated carbon nanotubes as highly efficient, universal-pH, oxygen reduction reaction catalysts. *Chem.—Eur. J.* **2019**, *25*, 2637–2644.

[34] Pan, J.; Song, S. Y.; Li, J. Q.; Wang, F.; Ge, X.; Yao, S.; Wang, X.; Zhang, H. J. Solid ion transition route to 3D S-N-codoped hollow carbon nanosphere/graphene aerogel as a metal-free handheld nanocatalyst for organic reactions. *Nano Res.* **2017**, *10*, 3486–3495.

[35] Li, Y. Q.; Huang, H. Y.; Chen, S. R.; Wang, C.; Liu, A. M.; Ma, T. L. Killing two birds with one stone: A highly active tubular carbon catalyst with effective N doping for oxygen reduction and hydrogen evolution reactions. *Catal. Lett.* **2019**, *149*, 486–495.

[36] Wang, T. H.; Tan, S. X.; Liang, C. H. Preparation and characterization of activated carbon from wood via microwave-induced $ZnCl_2$ activation. *Carbon* **2009**, *47*, 1880–1883.
[37] He, X. J.; Ling, P. H.; Yu, M. X.; Wang, X. T.; Zhang, X. Y.; Zheng, M. D. Rice husk-derived porous carbons with high capacitance by $ZnCl_2$ activation for supercapacitors. *Electrochim. Acta* **2013**, *105*, 635–641.
[38] Gadipelli, S.; Zhao, T. T.; Shevlin, S. A.; Guo, Z. X. Switching effective oxygen reduction and evolution performance by controlled graphitization of a cobalt–nitrogen–carbon framework system. *Energy Environ. Sci.* **2016**, *9*, 1661–1667.
[39] You, B.; Jiang, N.; Sheng, M. L.; Drisdell, W. S.; Yano, J.; Sun, Y. J. Bimetal-organic framework self-adjusted synthesis of support-free nonprecious electrocatalysts for efficient oxygen reduction. *ACS Catal.* **2015**, *5*, 7068–7076.
[40] Chen, Y. Z.; Wang, C. M.; Wu, Z. Y.; Xiong, Y. J.; Xu, Q.; Yu, S. H.; Jiang, H. L. From bimetallic metal-organic framework to porous carbon: High surface area and multicomponent active dopants for excellent electrocatalysis. *Adv. Mater.* **2015**, *27*, 5010–5016.
[41] Jiang, H. L.; Liu, B.; Lan, Y. Q.; Kuratani, K.; Akita, T.; Shioyama, H.; Zong, F. Q.; Xu, Q. From metal-organic framework to nanoporous carbon: Toward a very high surface area and hydrogen uptake. *J. Am. Chem. Soc.* **2011**, *133*, 11854–11857.
[42] Zhao, S. L.; Yin, H. J.; Du, L.; He, L. C.; Zhao, K.; Chang, L.; Yin, G. P.; Zhao, H. J.; Liu, S. Q.; Tang, Z. Y. Carbonized nanoscale metal-organic frameworks as high performance electrocatalyst for oxygen reduction reaction. *ACS Nano* **2014**, *8*, 12660–12668.
[43] Xia, B. Y.; Yan, Y.; Li, N.; Wu, H. B.; Lou, X. W.; Wang, X. A metal-organic framework-derived bifunctional oxygen electrocatalyst. *Nat. Energy* **2016**, *1*, 15006.
[44] Proietti, E.; Jaouen, F.; Lefèvre, M.; Larouche, N.; Tian, J.; Herranz, J.; Dodelet, J. P. Iron-based cathode catalyst with enhanced power density in polymer electrolyte membrane fuel cells. *Nat. Commun.* **2011**, *2*, 416.
[45] Fu, X. G.; Zamani, P.; Choi, J. Y.; Hassan, F. M.; Jiang, G. P.; Higgins, D. C.; Zhang, Y. N.; Hoque, M. A.; Chen, Z. W. *In situ* polymer graphenization ingrained with nanoporosity in a nitrogenous electrocatalyst boosting the performance of polymer-electrolyte-membrane fuel cells. *Adv. Mater.* **2017**, *29*, 1604456.
[46] Sharifi, T.; Hu, G. Z.; Jia, X. E.; Wågberg, T. Formation of active sites for oxygen reduction reactions by transformation of nitrogen functionalities in nitrogen-doped carbon nanotubes. *ACS Nano* **2012**, *6*, 8904–8912.
[47] Su, Y. H.; Jiang, H. L.; Zhu, Y. H.; Yang, X. L.; Shen, J. H.; Zou, W. J.; Chen, J. D.; Li, C. Z. Enriched graphitic N-doped carbon-supported Fe_3O_4 nanoparticles as efficient electrocatalysts for oxygen reduction reaction. *J. Mater. Chem. A* **2014**, *2*, 7281–7287.
[48] Wu, Z. S.; Yang, S. B.; Sun, Y.; Parvez, K.; Feng, X. L.; Müllen, K. 3D nitrogen-doped graphene aerogel-supported Fe_3O_4 nanoparticles as efficient electrocatalysts for the oxygen reduction reaction. *J. Am. Chem. Soc.* **2012**, *134*, 9082–9085.
[49] Zhang, J.; Wang, K. X.; Xu, Q.; Zhou, Y. C.; Cheng, F. Y.; Guo, S. J. Beyond yolk-shell nanoparticles: Fe_3O_4@Fe_3C core@shell nanoparticles as yolks and carbon nanospindles as shells for efficient lithium ion storage. *ACS Nano* **2015**, *9*, 3369–3376.
[50] Wei, Q. L.; Yang, X. H.; Zhang, G. X.; Wang, D. N.; Zuin, L.; Banham, D.; Yang, L. J.; Ye, S. Y.; Wang, Y. L.; Mohamedi, M. et al. An active and robust Si-Fe/N/C catalyst derived from waste reed for oxygen reduction. *Appl. Catal. B: Environ.* **2018**, *237*, 85–93.
[51] Xu, P.; Zhang, J.; Jiang, G. P.; Hassan, F.; Choi, J. Y.; Fu, X. G.; Zamani, P.; Yang, L. J.; Banham, D.; Ye, S. Y. et al. Embellished hollow spherical catalyst boosting activity and durability for oxygen reduction reaction. *Nano Energy* **2018**, *51*, 745–753.
[52] Wu, Z. X.; Liu, R.; Wang, J.; Zhu, J.; Xiao, W. P.; Xuan, C. J.; Lei, W.; Wang, D. L. Nitrogen and sulfur Co-doping of 3D hollow-structured carbon spheres as an efficient and stable metal free catalyst for the oxygen reduction reaction. *Nanoscale* **2016**, *8*, 19086–19092.